Benchmark Al-Cu Solidification Experiments in Microgravity and on Earth

THOMAS J. WILLIAMS and CHRISTOPH BECKERMANN

Predicting macrosegregation and grain structure, including the columnar to equiaxed transition (CET), in alloy solidification is an ongoing challenge. Gravity-driven melt convection and transport of unattached solid grains complicate such efforts. Cylindrical samples of aluminum alloys containing 4, 10, and 18 wt pct copper are solidified from the bottom upwards on Earth and in microgravity conditions aboard the International Space Station. The chosen alloys possess primary solid densities that are greater than, equal to, and less than their melt densities promoting different gravity-driven solid transport phenomena. Significant differences in grain structure are observed between microgravity and terrestrial samples. All microgravity samples are entirely equiaxed, while the terrestrial samples exhibit a CET. The columnar grains near the cooled surface in the terrestrial samples can only be attributed to melt convection. The Al-4 wt pct Cu terrestrial sample shows evidence of grain sedimentation, while the Al-18 wt pct Cu terrestrial sample exhibits the effects of grain floatation. Measurements of eutectic fraction and solute concentration in the samples show inverse segregation due to shrinkage-driven flow in all samples. Terrestrially solidified samples have areas of high solute concentration that are not uniformly distributed over the diameter, indicating the presence of melt convection. The eutectic and macrosegregation measurements generally have good correspondence. Temperature, grain structure, eutectic fraction, and macrosegregation data are presented as benchmark data to validate future modeling efforts. Heat flux boundary conditions on the sample are determined using thermal modeling. Thermal process parameters are calculated for all samples.

I. INTRODUCTION

GRAVITY plays an important role in metalcasting and solidification. Buoyancy-driven melt convection occurs in most castings due to thermal and solutal gradients that create local differences in fluid density. Unattached solids, such as equiaxed grains, may be advected by fluid flow or they may float or sediment due to their buoyancy in the melt. These transport processes create an uneven distribution of solute at the part scale known as macrosegregation. Melt convection and transport of free solid also influence the evolution of columnar grains, growth of equiaxed grains, and the columnar to equiaxed transition (CET). Macrosegregation and grain structure are significant factors in the quality of cast parts. Industrial production of cast metals can benefit from a better understanding of how gravity affects solidification.

Accurate numerical models validated with carefully performed experiments are necessary for understanding and predicting the casting process. Volume-averaged models have been created for columnar solidification that include the effect of melt convection.[1,2] Similar models have been developed for purely equiaxed solidification that account for melt convection, grain nucleation, and solid transport.[3–11] Joining the columnar and equiaxed models and predicting the CET are ongoing challenges. Models for mixed columnar-equiaxed solidification have been proposed without[12] and, more recently, with[13,14] consideration of melt convection and motion of unattached grains. Validating such solidification models requires high quality benchmark data from well characterized experiments employing a range of solidification conditions. Recent examples of such benchmarks are the experiments of References 15–19 for solidification of tin and select tin alloys under natural and forced melt convection conditions. The imposed cooling conditions and a large number of thermocouples provide a complete thermal profile of the samples. Grain structure and

THOMAS J. WILLIAMS and CHRISTOPH BECKERMANN are with the Department of Mechanical Engineering, The University of Iowa, Iowa City, IA, 52242. Contact e-mail: becker@engineering.uiowa.edu

macrosegregation data are also presented. These experiments lack corresponding cases free from melt convection. Additionally, as the experiments are focused on thermosolutally driven convection, transport of unattached equiaxed grains or dendrite fragments is outside their scope.

Aluminum-copper alloys are ideal for studying the effects of grain sedimentation or floatation on solidification microstructure development. Ganesan and Poirier[20] show that Al-Cu alloys with less than 10 wt pct Cu have a negatively buoyant primary solid, while alloys with greater than 10 wt pct Cu have a positively buoyant primary solid. Another beneficial property of Al-Cu alloys is that the Cu solute rejected during solidification causes an increase in the melt density. Therefore, when solidifying directionally in an upwards manner, the liquid metal is denser at the bottom of a casting due to lower temperatures and higher solute concentrations there. This thermosolutally stable configuration prevents large scale melt convection. Hence, buoyancy of unattached grains is the only driver of macroscopic transport in bottom-cooled experiments. Previous Al-Cu alloy solidification experiments have produced many interesting findings. Several of these investigations also demonstrate potential difficulties in studying solid transport in these alloys. Soltani et al.[21] have performed upwards, downwards, and horizontal solidification experiments using very thin Al-20 wt pct Cu samples in a Bridgman type furnace. In situ observations during the experiments reveal the effects of grain floatation on the development of the microstructure. For upwards solidification, equiaxed grains can float out of the narrow solidification zone and remelt. However, some grains become trapped due to the thinness of the sample. Yasuda et al.[22] have observed directional solidification in Al-5, 10, and 15 wt pct Cu alloys. They find no evidence of equiaxed grain nucleation in the 5 wt pct Cu alloy and suggest that such nucleation is difficult in any Al alloy with less than 5 wt pct Cu. Rerko et al.[23] have conducted separate top- and bottom-cooled solidification experiments using Al-1 and 10 wt pct Cu alloys. Each combination of alloy and cooling direction is found to produce a unique microstructure due to different primary solid buoyancies and melt convection patterns. Since a bottom-cooled Al-10 wt pct Cu alloy has a thermosolutally stable melt and a neutrally buoyant primary solid during solidification, no macroscale transport is expected. However, Zimmermann et al.[24] have found that dendrite fragments from deep within the mushy zone can still float to the columnar front and cause significant changes in the CET between thin and bulk samples. They also find that in one case, columnar grains grew inclined relative to the sample axis. The inclined growth creates small convection cells near the solidification front that suppress the nucleation and growth of equiaxed grains. Burden et al.[25] have observed a non-planar solidification front in quenched bulk Al-Cu samples that are bottom cooled. They propose that small transverse thermal gradients produce convection cells that grow to sufficient strength to alter the solidification front. Reinhart et al.[26] confirm such a phenomenon through in situ observations in a solidification experiment designed to be thermosolutally stable. In summary, it is clear that Al-Cu alloys are well suited for the study of grain sedimentation and floatation. However, experiments designed to be thermosolutally stable do not necessarily eliminate melt convection. Moreover, experiments using an alloy with a neutrally buoyant primary solid may still show some motion of unattached grains.

Microgravity experiments are necessary to effectively eliminate buoyancy-driven phenomena during solidification. Microgravity can be achieved for a short time using sounding rockets or drop tubes. This may be sufficient for thin samples that solidify quickly.[27,28] Ngomesse et al.[29] have observed in situ solidification of an Al-20 wt pct Cu alloy with grain refiner in a microgravity environment using a sounding rocket. The microstructures are significantly different from those obtained in comparable terrestrial experiments.[21] Longer duration microgravity is necessary for bulk samples. It can be achieved using the materials science facilities aboard the International Space Station (ISS). Microgravity experiments have been conducted by Liu et al.[30] for bulk samples in a Bridgman type furnace using an Al-7 wt pct Si alloy. The experiments employ a decrease in temperature gradient and a change in pulling speed to trigger a CET in samples with and without grain refiner. In a nominally identical setup on Earth, Li et al.[31] have conducted a corresponding terrestrial experiment for a case without grain refiner or pulling speed increase. They compare results from the microgravity and terrestrial experiments to elucidate the effects of gravity on the grain structure and the CET. They find that convective effects promote columnar growth by alleviating the blocking effects of equiaxed grains. These experiments provide important benchmark data for understanding the effect of gravity-driven transport on the CET. However, Bridgman furnace experiments are designed to focus narrowly on the solidification front in an effectively semi-infinite domain. Some phenomena, such as the pile-up of floating grains at the top of a casting, are difficult to produce under Bridgman conditions. Additionally, characterizing the initial conditions and modeling the transport phenomena in non-steady-state Bridgman furnace experiments are more complex than for an experiment using initially fully melted alloys and end-cooled bulk samples of finite extent.

The goal of the present work is to conduct corresponding microgravity and terrestrial benchmark solidification experiments using end-cooled cylindrical samples of Al-Cu alloys with negatively, neutrally, and positively buoyant primary solid. Temperature data from the experiments are recorded with thermocouples. Grain structure characterization is accomplished via metallography and micrograph analysis. Solute segregation data are acquired using spectroscopy techniques and micrograph analysis. The results are compared to elucidate the effects of gravity on grain structure and macrosegregation. The temperatures as well as the grain structure, eutectic distribution, and macrosegregation measurements are presented as benchmark data. In order to facilitate future modeling efforts, thermal
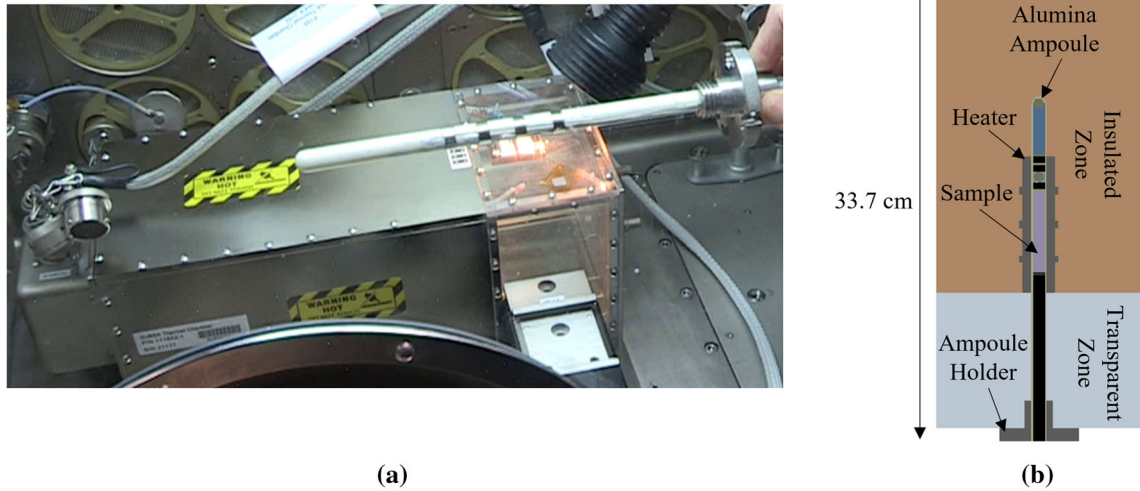
Fig. 1—The SUBSA furnace: (*a*) image during ampoule insertion on board the International Space Station and (*b*) schematic of the cross section through the ampoule centerline.

boundary conditions for the sample are determined from a thermal model of the full furnace. Axial temperature gradients, isotherm velocities, and cooling rates in the samples are calculated to characterize the experiments in the absence of convection and transport of unattached grains.

II. EXPERIMENTS

Cylindrical samples of Al-4, 10, and 18 wt pct Cu alloys are solidified from the bottom on Earth and in microgravity. The chosen alloys have primary solids with negative, neutral, and positive buoyancy in the melt. During the experiments, the cylindrical samples are fully melted and allowed to thermally stabilize before cooling at a controlled rate. The bottom-upwards cooling significantly limits thermosolutally driven melt convection in the terrestrially solidified samples. Microgravity experiments provide results free from the influence of buoyancy. After the experiments, grain structure, CET, eutectic distribution, and macrosegregation are characterized for each sample.

A. Furnace and Ampoule Setup

The Solidification Using a Baffle in Sealed Ampoules (SUBSA) furnace,[32] developed by NASA, melts and solidifies samples held within alumina ampoules inserted along its central axis. Twin furnaces are used to conduct solidification experiments in the presence of gravity on Earth and in microgravity aboard the ISS. Figure 1(a) shows the microgravity furnace during ampoule insertion. The SUBSA furnace measures 33.7 cm in length from the bottom of the ampoule holder to the furnace top. Temperature monitoring and furnace control are accomplished in real-time on the ground. A cross section of a thermal model of the furnace interior with an ampoule inserted is shown in Figure 1(b). The furnace is oriented vertically on Earth for the present experiments.

It is divided into two main regions, a transparent zone and an insulated zone. The ampoule is passively cooled through the transparent zone and the ampoule holder at the bottom. The insulation zone can be further subdivided into the actively heated zone, which contains the heater, and the passively heated zone above the heater. The heater consists of resistive wire wrapped around a stainless steel core. The heat input is managed by software to allow heating and cooling at well controlled rates.

The design of the sample ampoules is shown in Figure 2 and is described here according to the vertical alignment in the terrestrial furnace where the ampoule holder is at the bottom. The alumina ampoule has an inner diameter of 9.5 mm. Starting from the ampoule holder and moving upwards, there is a graphite rod with a length of 123 mm, capped by a 2 mm thick piece of graphite felt. The rod and felt provide significant cooling to the sample due to the relatively high thermal conductivity of graphite. They also position the alloy sample within the ampoule and therefore the furnace. The flexibility of the graphite felt prevents possible leakage of molten metal. The cylindrical alloy sample sits above the graphite felt and has a nominal diameter of 9 mm which, due to solidification shrinkage, is smaller than the ampoule inner diameter of 9.5 mm. The nominal length of the sample is 60 mm. The sample length and position within the furnace are chosen to ensure complete melting and solidification from the lower sample end. Above the sample there is a combination of graphite spacers, alumina spheres, alumina papers, and a spring. This combination of materials serves several purposes. The spring allows for sample expansion due to heating and melting but also provides a compressive force during cooling that is intended to limit shrinkage defects. The spring is placed as high in the ampoule as possible to limit direct exposure to the actively heated zone of the furnace. The combination of graphite spacers and alumina spheres and papers positions the spring outside the actively heated zone.
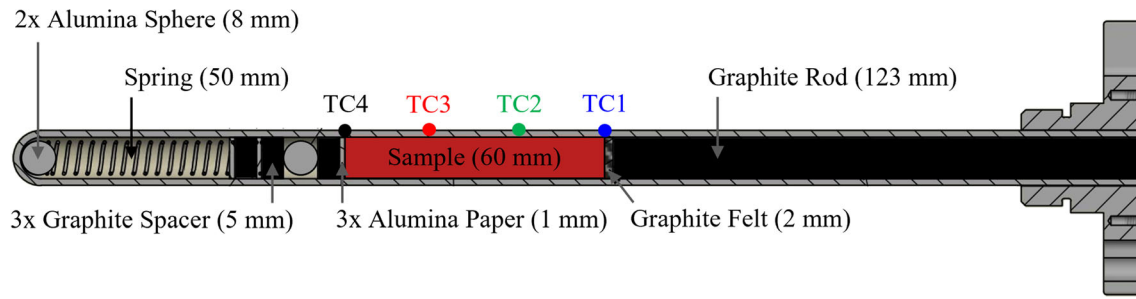
Fig. 2—Ampoule configuration and thermocouple placement. Thermocouples are placed on the ampoule exterior at 0, 20, 40, and 60 mm from the sample end.

Table I. Material Properties, Phase Diagram Properties, and Other Relevant Quantities for Al-Cu Alloys Used in this Work

Property	Al-4 wt pct Cu	Al-10 wt pct Cu	Al-18 wt pct Cu
Al Melting Point, T_f (°C)	660.5		
Liquidus Temperature, T_{liq} (°C)	649.81	633.36	609.2
Eutectic Temperature, T_{eut} (°C)	548.01		
Scheil Eutectic Fraction, g_{eut}	0.0916	0.2547	0.4928
Partition Coefficient, k_{avg}	0.125	0.129	0.138
Liquidus Slope, m_l (K/wt pct)	− 3.47	− 3.42	− 3.40
Liquid Density, ρ_l (kg/m^3)	2446	2582	2767
Primary Solid Density, ρ_{ps} (kg/m^3)	2571	2587	2620
Bulk Solid Density, ρ_s (kg/m^3)	2648	2797	3009
Shrinkage Factor, β	0.082	0.083	0.087

The presence of multiple interfaces and the low thermal conductivity of the alumina also limit heat transfer from the sample top. The flexible alumina paper aids in preventing leakage of molten metal. Type-K thermocouples (TCs) are placed on the outside of the alumina ampoule at 0, 20, 40, and 60 mm relative to the sample bottom and labeled TC1-4, respectively. They are fixed in place using an alumina cement. Temperature readings from the TCs are logged at a frequency of 1 Hz.

Sample cylinders of Al-4, 10, and 18 wt pct Cu were created using 99.9 pct pure aluminum and copper parent materials and provided by NASA's Marshall Space Flight Center. No grain refiner was used in any of the samples. The transport of refining particles can have significant effects on the final microstructure.[33] Six ampoules in total were constructed, two for each of the three alloys. Alloy phase diagram properties, material properties, and other relevant quantities are listed in Table I. The phase diagram properties were determined using the software JMatPro.[34] The software calculates the final eutectic fraction assuming Scheil-type solidification with variable partition coefficients and liquidus slopes. The partition coefficient in Table I is calculated as the average partition coefficient between an alloy's liquidus temperature and the eutectic temperature. The constant liquidus slope in Table I is obtained from the rearranged Scheil equation:[35]

$$m_l = \frac{T_{eut} - T_f}{C_0 g_{eut}^{(k_{avg}-1)}} \quad [1]$$

where the values for all variables on the righthand side of Eq. [1] are from Table I and C_0 is the alloy composition in wt pct Cu. Liquid and primary solid densities, listed in Table I, are calculated according to Equations [5–7, 10] in Reference 20 using the initial composition and liquidus temperature. Comparing the liquid density and primary solid density values in Table I demonstrates that Al-4, 10, and 18 wt pct Cu alloys have negatively, neutrally, and positively buoyant primary solids, respectively. The bulk solid density, which is the density of the solid after eutectic solidification, is calculated using the primary solid density and Scheil eutectic fraction from Table I as well as the eutectic density of 3409 kg/m^3 provided in Reference 20. It must be noted that even though the primary solid of Al-18 wt pct Cu is less dense than the liquid, the bulk solid is still more dense than the melt. The solidification shrinkage factor is calculated as $\beta = (\rho_s/\rho_l) - 1$ using the corresponding values from Table I. All alloys used in this study have a solidification shrinkage factor between 0.08 and 0.09. Therefore, all chosen alloys shrink during solidification, regardless of the primary solid density.

B. Experimental Procedure

In order to standardize the experiments, all samples were heated in the SUBSA furnace by increasing the furnace temperature at 5 °C/minute until TC4 reached 100 °C above a given alloy's liquidus temperature. In the Al-10 wt pct Cu cases, TC1 did not read above the liquidus temperature, although TC4 had reached the

specified temperature. Therefore, these samples were further heated until TC1 was above the liquidus temperature to ensure full melting. Samples were held for 30 minute in the molten state to stabilize the internal temperatures. Finally, samples were cooled and solidified by decreasing the furnace temperature at a rate of 5 °C/minute. When the furnace reached approximately 300 °C, it was switched off entirely. Microgravity experiments were performed first so that any unforeseen deviations from protocol could be replicated in the terrestrial experiments. Terrestrial samples were solidified with the furnace oriented vertically to ensure bottom-upwards solidification and limit thermosolutally driven melt convection.

C. Sample Characterization

Following the experiments, samples were carefully removed from their ampoules. Any issues such as broken or misplaced TCs were logged. After sample removal, all samples were sectioned along the cylinder axis, mounted in epoxy, and metallographically polished. Samples were then electrolytically etched to reveal the grain structure. The etchant used was the Barker etchant, which is approximately 2.5 vol pct tetrafluoroboric acid (HBF_4) in deionized water. For Al-Cu samples, 17 to 25 V DC was applied for 120 to 150 s. Voltage and time increased with decreasing Cu content. After etching, the samples were imaged at 200 times using polarized optical microscopy, which produces color contrast based on different grain orientation. Composite images of the entire sample are produced from the smaller individual images. The composite images have square pixels of side length 2 to 7 μm depending on the amount of compression during the image merging process. Following this, the samples were metallographically polished again and Scanning Electron Microscope (SEM) imaging was conducted at 100 times for all samples. Concurrently, Energy Dispersive X-ray Spectroscopy (EDX) scans were taken of the full field of view (FOV) of each individual imaged area, measuring 1.03 mm by 0.77 mm. The scans quantified the average solute concentration for the entire surface within a FOV.

The polarized microscope composite images were analyzed to determine grain size and to map the area fraction of eutectic across the sample. Grain size was characterized using a simple intercept method. Lines were drawn manually across the diameter at approximately regular intervals along the axis. The number of grain boundary intercepts on each line was counted. The mean radial intercept length was calculated as the length of each line divided by the number of grain boundary intersections with that line. While the mean radial intercept length should not be taken as a true grain size, it characterizes grain size changes along the axis and serves as a starting point for modeling efforts.

The eutectic area fraction or eutectic percentage was measured from the composite polarized micrographs using the software ImageJ.[36] The images, including the empty border area around the sample, were converted to 8-bit gray scale, then binarized, and any pores or empty

space were marked Not-A-Number (NaN). Some samples had areas that were not successfully etched and were marked NaN because they cannot be successfully analyzed for eutectic fraction. The binarization grayvalue threshold was set so the resulting average eutectic percentage for the whole sample is equal to the Scheil eutectic fraction from Table I for a given alloy. The authors acknowledge that this assumption is only approximate, particularly in the presence of convection. An example comparison of a cutout from the Al-18 wt pct Cu μg polarized micrograph before and after binarization is shown in Figure 3 to demonstrate the relative accuracy of the process. The result of the binarization process was an image with pixel values of 0 for eutectic material, 1 for primary material, or NaN for reasons described previously. Once a properly binarized image was obtained, complete with NaN masking, eutectic percentage was mapped using a box averaging technique. Boxes here are simply squares. A grid of square boxes was digitally overlaid on the binarized images and the area fraction of eutectic pixels was determined within each box. This method of box averaging was chosen, rather than a sliding average, to create a measurement grid comparable to the one for the EDX data. NaN pixels were removed from the eutectic fraction calculation. However, if more than 20 pct of the pixels in a box were marked NaN, the eutectic fraction for that entire box was set to NaN, which prevented issues caused by sparsely populated boxes. A grid could not be fit exactly to the samples, as none of the cross sections were perfectly rectangular. Therefore, the side length of the boxes was set individually for each image such that 12 boxes span the binarized image in the sample diameter direction, including the empty space around the edge of the sample. This resulted in a box side length of approximately 0.75 mm or 100 to 375 pixels, though the exact value varied between images based on the amount of empty space bordering the sample. This box side length is similar to the shorter dimension of the EDX acquisition field. Additional box sizes were investigated in Reference 37. Larger boxes smoothed out some features while smaller boxes introduced excessive scatter in the measurements. The results of the eutectic measurements were processed into 2D maps. The inclusion of the empty space from the binarized images produced a perimeter of NaN-valued boxes around every map. Additionally, the eutectic percentage results were averaged in the diameter direction to create profiles of eutectic percentage along the sample axis.

Individual EDX measurements determined the average solute concentration for the full SEM FOV, 1.03 mm by 0.77 mm. Individual fields were then joined to create a solute concentration map for the whole sample. This characterizes macrosegregation by averaging solute concentrations for primary and eutectic material within the FOV and then observing the heterogeneity of the averaged values on the sample scale. Like the eutectic measurements, some EDX measurement areas contained large flaws or empty space. Measurements for such areas were marked NaN if approximately 20 pct or more of the measured area
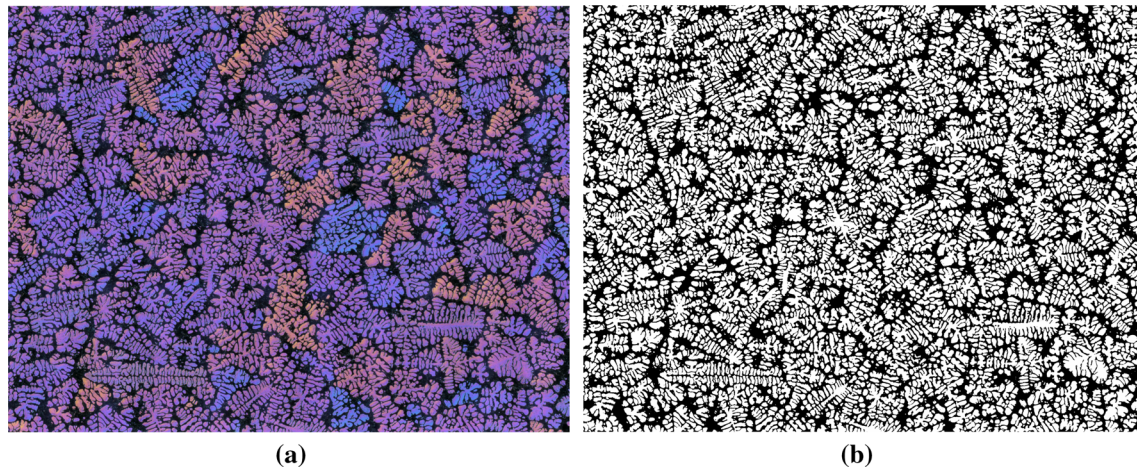
(a)   **(b)**

Fig. 3—An example of the binarization process showing (*a*) an approximately 7 mm by 9 mm cutout of the Al-18 pct Cu μg polarized micrograph and (*b*) the same cutout after binarization.

was empty or contained a flaw. Unlike for the eutectic measurements, the amount of flawed or empty area was determined by inspection of the corresponding SEM micrograph rather than by digital quantification. The EDX results were calibrated, because scanning a large FOV of an inhomogeneous material results in a loss of accuracy. Calibration was accomplished by dividing individual results by the average measured solute concentration and multiplying by the nominal composition of a given sample. The Al-4 wt pct Cu μg and 1 g samples had sample averages of 4.51 and 4.43 wt pct Cu, respectively, prior to calibration. The Al-10 wt pct Cu μg and 1 g sample averages before calibration were 8.56 and 8.58 wt pct Cu, respectively. The pre-calibration sample averages for the Al-18 wt pct Cu μg and 1 g samples were 15.97 and 16.21 wt pct Cu, respectively. NaN's were excluded from the sample averaging. The original EDX acquisition grids were not always well aligned with the sample dimensions and used non-square measurement areas. To rectify this issue, the calibrated EDX results, for all samples, were re-mapped to a sample-aligned square box grid that is nearly the same as the eutectic measurement box grid to facilitate comparison of the two quantities. Re-mapping was accomplished by sampling the calibrated EDX data with an array of points spaced such that 60 sampling points span the diameter direction of the calibrated EDX data map. The chosen number of points places 5 to 6 sampling points over the 1.03 mm measurement area width by 4 to 5 sampling points over the 0.77 mm height. Each point was assigned the value of the EDX measurement area it fell within. The sampling points were then be averaged in a 5 by 5 pattern to create a square box grid with 12 boxes spanning the diameter direction, the same number of square boxes as for the eutectic measurements. Given the different sources and methods used to create these two box grids, there were some small discrepancies between them. However, results show the differences were not significant. Similar to the eutectic measurements, the square box averaged

EDX data was also averaged across the diameter direction to create a profile of solute concentration along the axis.

As the 2D maps of eutectic fraction and solute content are of different quantities, they can only be qualitatively compared. To create a quantitative comparison, the diameter averaged eutectic percentage measurements were transformed to solute concentrations using a rearranged form of the Scheil equation with constant liquidus slope and partition coefficient:

$$C = \frac{T_{\text{eut}} - T_{\text{f}}}{m_{\text{l}} g_{\text{eut}}^{(k_{\text{avg}} - 1)}} \qquad [2]$$

where C is the resulting solute concentration, g_{eut} is the measured eutectic fraction, and the other parameters are from Table I. As in the micrograph binarization process, this raises the issue of assuming Scheil solidification, but here it is simply a point of comparison for the two data sources. Both the transformed eutectic profile and the calibrated EDX solute concentration profile were normalized using their respective sample averages prior to comparison.

III. RESULTS AND DISCUSSION

Thermocouple readings, grain structures, eutectic distributions, and solute distributions are presented and discussed here separately. Eutectic and solute distributions are compared directly to assess the reliability of the measurement methods.

A. *Thermocouple Measurements*

Measured temperatures for all experiments are shown in Figure 4. These temperatures are also included in an electronic supplementary spreadsheet in the online version of this article. Time is labeled such that cooling from the high temperature hold begins at 0 s. The
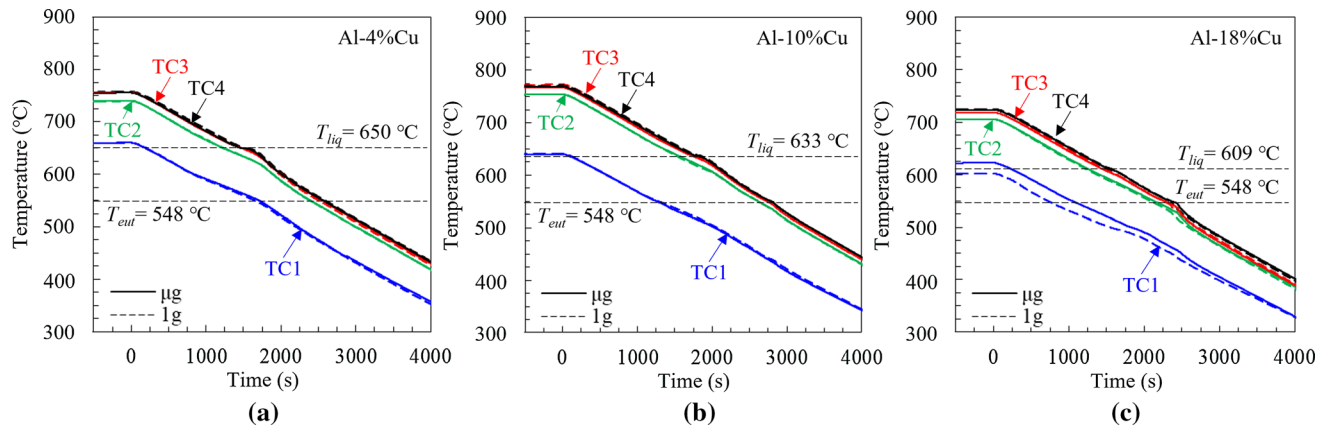
Fig. 4—Measured temperatures for the (*a*) Al-4 wt pct Cu, (*b*) Al-10 wt pct Cu, and (*c*) Al-18 wt pct Cu experiments. Cooling begins at 0 s.

heating portion of the histories is excluded for brevity. The most notable feature of the temperature results is that, for each alloy, the microgravity and terrestrial temperature results are nearly identical. The one exception to this is in Figure 4(c) at TC1 in the Al-18 wt pct Cu terrestrial (1 g) case. In this case, TC1 recorded a sudden drop in temperature before the timeframe of Figure 4(c). This temperature drop is attributed to a delamination issue with the cement holding TC1 in place. No other sharp temperature changes were noted. As noted in Section II–B, the Al-10 wt pct Cu samples required additional heating so that TC1 would exceed the liquidus temperature. This is visible in Figure 4(b) as TCs 2 to 4 are at higher initial temperatures than in Figure 4(a) for the Al-4 wt pct Cu alloy. Lower initial temperatures would be expected for the Al-10 wt pct Cu alloy as it has a lower liquidus temperature than the Al-4 wt pct Cu alloy. This indicates some measurement error at TC1 for the Al-10 wt pct Cu alloys, the source of which is unknown. For each alloy, the corresponding microgravity and terrestrial experiments can be considered to have the same heat input and extraction. Therefore, any differences in the grain structure or macrosegregation can be attributed directly to the presence or absence of gravity. It is important to recall that the temperatures are recorded on the exterior of the ampoule. Therefore, the thermocouple data are not straightforwardly useful for future modeling efforts. This is addressed later in this work.

B. *Grain Structure*

Polarized micrographs of the electrolytically etched samples are shown in Figures 5, 6, and 7 for the Al-4, 10, and 18 wt pct Cu samples solidified in microgravity (μg) and on Earth (1 g). The full resolution images are included as electronic supplementary Figures S1 to S6 in the online version of this article. The electrolytic etching process produces color contrast between grains of a single sample. Different color schemes between samples are not physically significant. Small areas where etching failed near sample ends are indicated in Figures 5 and 6(b). All samples exhibit shrinkage pores of varying size.

Most of the pores are small and can be disregarded. Larger cavities along the sample exterior, such as in the Figure 6(b), are only present over part of the circumference. Large internal shrinkage cavities are present in Figures 5(b) and 7(b). Shrinkage pores likely formed near the end of solidification when the grain structure has been established and the effects of buoyancy have become negligible. Mean radial intercept length profiles that characterize grain size are shown in Figure 8.

Observing all the sample micrographs and grain size profiles together, two significant features stand out. The first important difference between the μg and 1 g samples for each alloy is the presence or absence of columnar grains. The μg samples exhibit a fully equiaxed grain structure. In contrast, the 1 g samples have columnar grains near the sample bottom that progressively transition to a fully equiaxed structure in the upper portions of the samples. Equiaxed grains in the samples may have arisen *via* fragmentation or nucleation; however, the exact mechanism is unknown and outside the scope of this investigation. The difference in grain structure between μg and 1 g samples can only be explained by the presence of melt convection in the 1 g samples. Floatation or sedimentation of grains is unlikely to explain the presence of the columnar grains because they are present in all 1 g samples, regardless of the buoyancy of the primary solid. Due to the bottom-up mode of solidification, the amount of melt convection is likely small. However, as reviewed previously, small convection cells can still form near the dendrite tips and could contribute to the growth of columnar grains. In the present experiments, there are non-negligible radial heat fluxes on the sample circumference near the bottom (see Sect. 4.2) that can also contribute to the initiation of melt convection in the 1 g samples. The second key distinction between the μg and 1 g samples is the variation in equiaxed grain size. Figure 8 shows that the equiaxed grain sizes in all μg samples are similar except for a small increase toward the sample top in the Al-4 and 10 wt pct Cu samples. On the other hand, the fully equiaxed regions of the Al-4 and 18 wt pct Cu 1 g samples exhibit highly variable grain sizes. The Al-10 wt pct Cu 1 g sample has the same
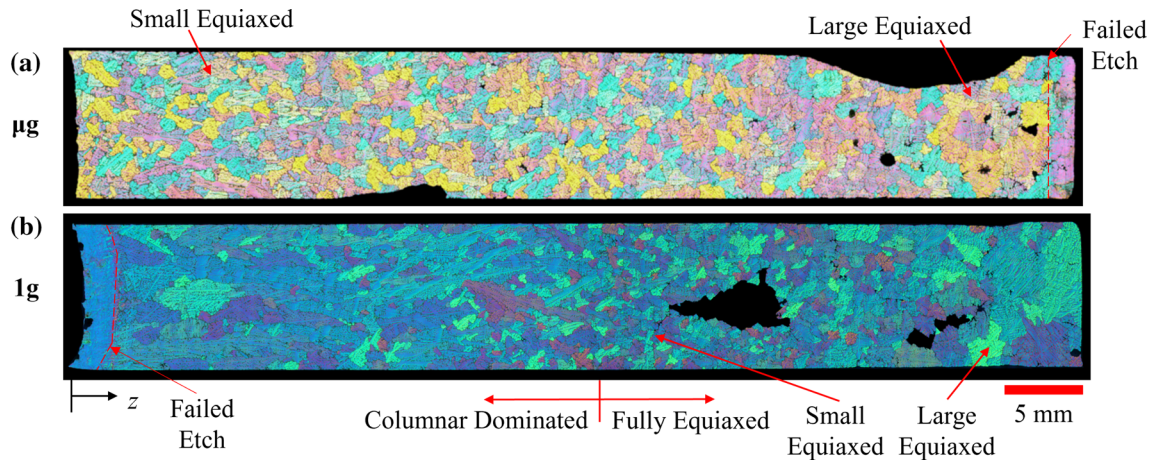
Fig. 5—Micrographs of the electrolytically etched Al-4 wt pct Cu (*a*) μg and (*b*) 1 g samples.
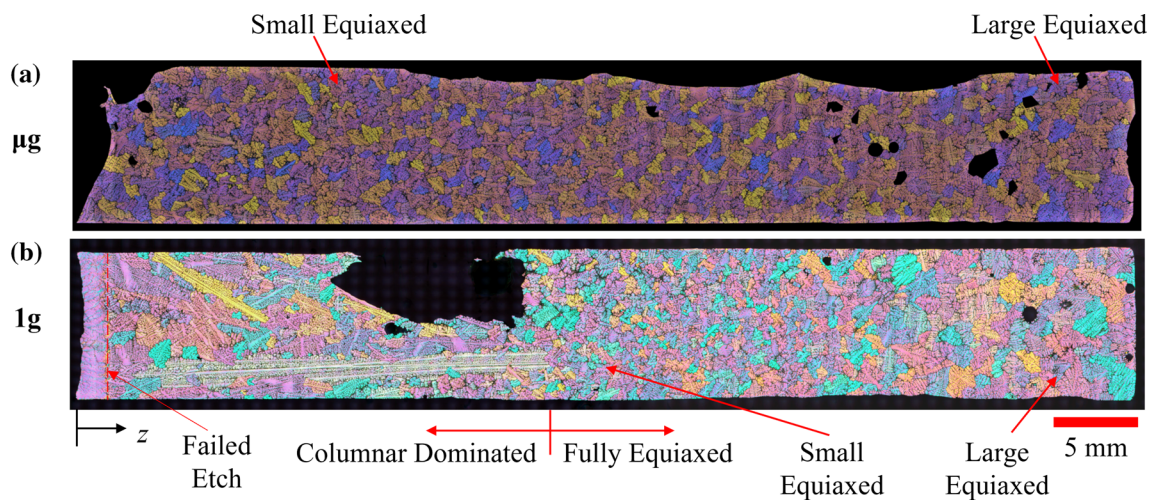

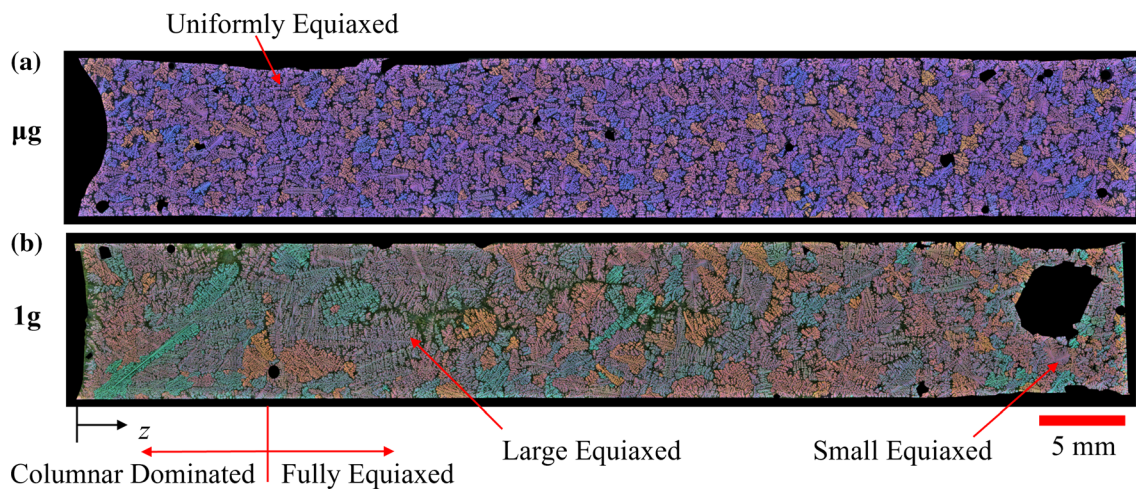Fig. 6—Micrographs of the electrolytically etched Al-10 wt pct Cu (*a*) μg and (*b*) 1 g samples.

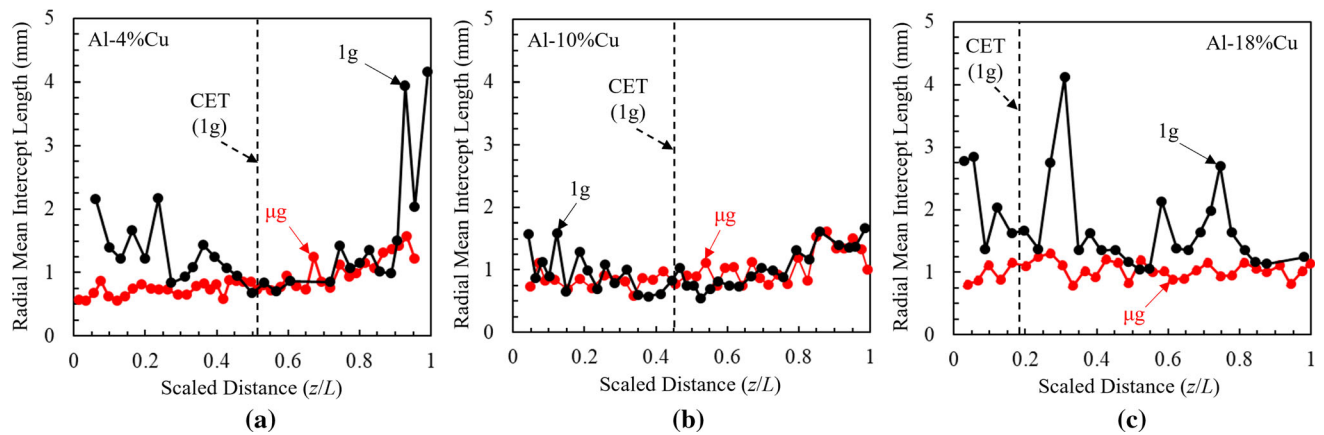Fig. 7—Micrographs of the electrolytically etched Al-18 wt pct Cu (*a*) μg and (*b*) 1 g samples.

Fig. 8—Radial mean intercept length profiles, representing the grain size, for the (*a*) Al-4 wt pct Cu, (*b*) Al-10 wt pct Cu, and (*c*) Al-18 wt pct Cu samples.

grain size and variation as the Al-10 wt pct Cu μg sample. These observations are discussed for each of the alloys individually below.

The fully equiaxed grain structure of the Al-4 wt pct Cu μg sample [Figures 5(a) and 8(a)] exhibits a slight increase in size toward the end of the sample, which may be attributed to a decreasing cooling rate. On the other hand, the Al-4 wt pct Cu 1 g sample grain structure can be divided into a columnar dominated region from 0 to approximately 3.3 cm and a fully equiaxed region from 3.3 cm to the sample top [Figure 5(b)]. The division between columnar dominated and fully equiaxed regions can be considered as the CET location for the 1 g sample. However, the columnar dominated region does contain some smaller elongated grains and several equiaxed grains which indicate a progressive rather than a sharp CET. It is not clear whether the equiaxed grains between the columnar grains fragmented from dendrite arms or nucleated further up in the sample before sedimenting. The grains in the fully equiaxed region greatly increase in size toward the sample top such that two large grains span the entire sample width at the top in Figure 5(b). Such grains do not exist in the top 10 pct of the μg sample and are clear evidence of grain sedimentation. The primary solid in Al-4 wt pct Cu is denser than the molten metal. When equiaxed grains nucleate in the undercooled liquid, smaller unattached grains sediment downwards. Such sedimentation results in numerous small equiaxed grains lower in the equiaxed region and fewer but larger grains near the sample top.

The Al-10 wt pct Cu μg sample also has a fully equiaxed grain structure with a slight increase in grain size toward the sample end [Figures 6(a) and 8(b)]. Figure 6(b) shows that the Al-10 wt pct Cu 1 g sample has a columnar dominated region from 0 to approximately 2.8 cm which coincides with the end of a long columnar grain. After the CET at 2.8 cm, the grain structure becomes fully equiaxed for the remainder of the sample. Again, the CET can be characterized as progressive because the columnar dominated region contains many smaller elongated and equiaxed grains. In the fully equiaxed region of the Al-10 wt pct Cu 1 g

sample the grain size increases slightly toward the sample top [Figure 8(b)]. This increase is the same as the increase in the μg sample, which implies that neither sedimentation nor floatation occurred in the 1 g sample. This result is expected because Al-10 wt pct Cu has a neutrally buoyant primary solid.

Finally, the Al-18 wt pct Cu μg sample shows a remarkably uniform equiaxed grain size despite the decreasing cooling rate toward the sample end [Figures 7(a) and 8(c)]. The Al-18 wt pct Cu 1 g sample [Figure 7(b)] shows large columnar and elongated equiaxed grains near the sample bottom from 0 to approximately 1.1 cm. After the end of the progressive CET at 1.1 cm, the 1 g sample is entirely equiaxed. Unlike all other samples, there is a strong decrease in equiaxed grain size toward the sample top. This increase can only be explained by the floatation of equiaxed grains [Figure 8(c)]. The primary solid in Al-18 wt pct Cu is less dense than the melt so nucleated equiaxed grains float upwards. Floating grains accumulate at the sample top, reducing the grain size there. Correspondingly, there are fewer but larger grains lower in the sample.

In summary, the present experiments reveal two important effects of gravity in metal solidification. First, columnar grains and a progressive CET are exhibited by all 1 g samples, but not by any μg samples. This difference indicates that melt convection has a significant effect on the grain structure of the 1 g samples. Second, the equiaxed grains in the Al-4 and 18 wt pct 1 g samples exhibit clear evidence of sedimentation and floatation, respectively, while the Al-10 wt pct 1 g sample does not.

C. *Eutectic Distribution*

Two-dimensional maps of the eutectic area percentage are shown in Figures 9, 10, 11. The area within the black boundary is the same for the eutectic maps and the corresponding micrographs. As a result, the boxes around the perimeter of the maps are all NaN-valued and appear black. Areas of failed etch or large shrinkage
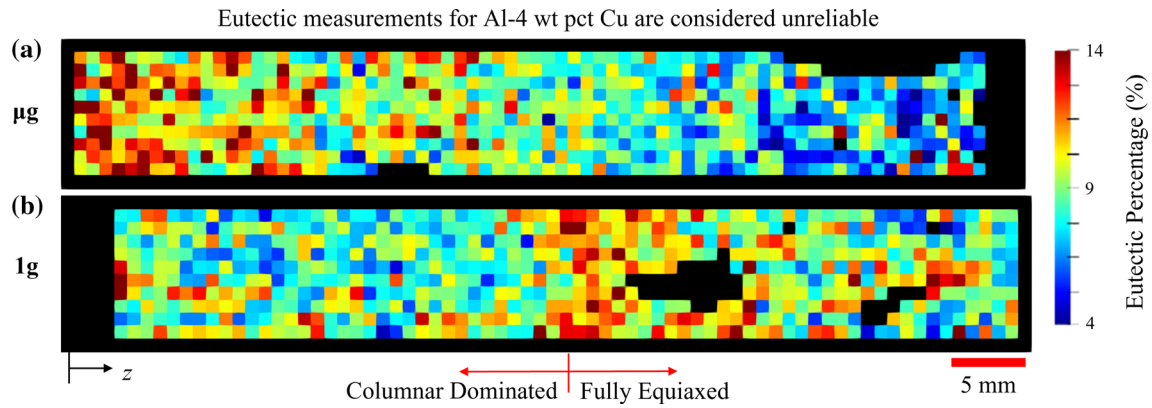
Fig. 9—Eutectic percentage maps for the Al-4 wt pct Cu (*a*) μg and (*b*) 1 g samples. These measurements are considered unreliable.
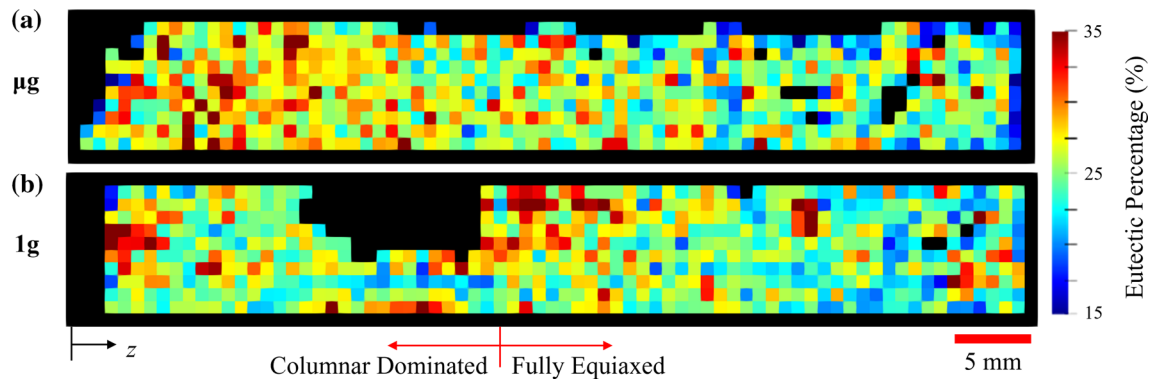

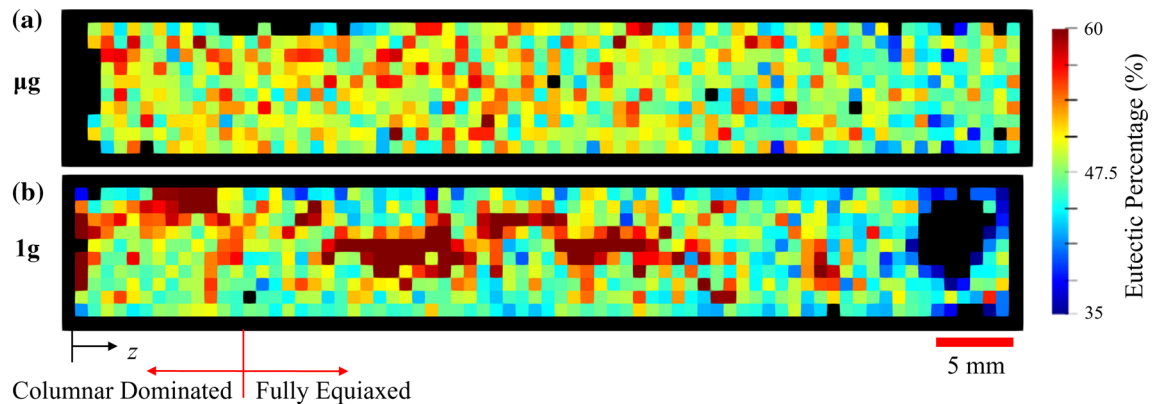Fig. 10—Eutectic percentage maps for the Al-10 wt pct Cu (*a*) μg and (*b*) 1 g samples.

Fig. 11—Eutectic percentage maps for the Al-18 wt pct Cu (*a*) μg and (*b*) 1 g samples.

have been blacked out *via* NaN masking. Axial profiles of the diameter averaged eutectic percentage are shown in Figure 12.

A few features stand out when viewing all of the eutectic measurements together. Figure 12 shows that in all μg samples the eutectic percentage decreases toward the sample end. This must be caused by

shrinkage-driven flow of solute rich melt that results in so called inverse segregation toward the cooled surface.[35] An increase in the solute content of the melt will produce a higher eutectic area fraction. The eutectic fraction maps for the 1 g samples have other features which are discussed below.
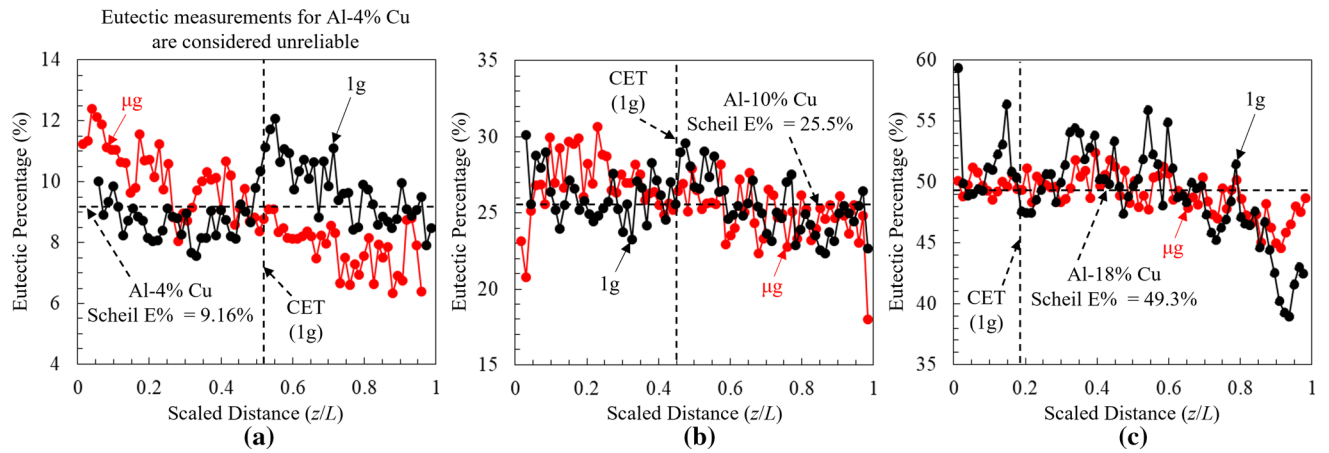
Fig. 12—Axial profiles of diameter averaged eutectic percentage for the (a) Al-4 wt pct Cu (considered unreliable), (b) Al-10 wt pct Cu, and (c) Al-18 wt pct Cu samples.

While the Al-4 wt pct Cu μg sample exhibits the steadily decreasing eutectic percentage discussed above, the 1 g sample shows an initially decreasing eutectic percentage interrupted by a sharp increase at the termination of the progressive CET near sample mid-height [Figure 12(a)]. The eutectic percentage decreases in the upper half of the sample but remains higher than in the lower half of the sample. Measurement of the eutectic fraction is difficult in the Al-4 wt pct Cu alloy because of the low overall eutectic fraction and because the eutectic within grains is not as easily detected as the eutectic between the grains. Equiaxed grains have more intergranular area which results in the higher eutectic percentage measured after the CET. These issues make the eutectic fraction measurements unreliable for the Al-4 wt pct Cu alloy, which is further corroborated by the comparison with the macrosegregation measurements in Sect. 3.5.

The Al-10 wt pct Cu μg and 1 g samples have similar eutectic percentage profiles that decrease toward the sample top [Figure 12(b)]. This similarity is evidence of inverse segregation in both samples. It also indicates negligible floatation or sedimentation of unattached grains in the 1 g sample. There are several isolated pockets of high eutectic percentage in the 1 g sample eutectic percentage map [Figure 10(b)] that are not present in the μg eutectic percentage map [Figure 10(a)]. These pockets are found at the sample bottom, at the sample edge above the large void, and in the sample cross section approximately 15 mm from the top. As the solid is neutrally buoyant in this case, melt convection is the most likely cause of the pockets.

The Al-18 wt pct Cu μg sample shows a uniform distribution of eutectic in the lower half of the sample, while the upper half shows a decreasing eutectic percentage toward the end [Figure 12(c)]. This pattern of inverse segregation is different from the other two alloys because the Al-18 wt pct Cu alloy expands during primary solidification and only shrinks during eutectic solidification (Table I). The 1 g sample shows a similar eutectic fraction profile to the μg sample but has a significantly lower eutectic percentage in the top 15 pct of the sample

[Figure 12(c)]. This can be attributed to the accumulation of solute-poor primary solid grains that floated to the top of the 1 g sample. The strong spikes in the 1 g eutectic percentage profile in Figure 12(c) can be explained by pockets and regions of high eutectic percentage that do not extend over the entire cross section of the sample. In the columnar area of the sample in Figure 11(b), there are pockets of high eutectic percentage at the sample bottom and on the sample edge that strongly indicate the presence of melt convection during solidification. In the equiaxed area of the sample a large region of high eutectic percentage is present along the axis of the sample. This region may be due to a combination of melt convection and grain floatation.

In all samples, the measurements of eutectic area fraction demonstrate inverse segregation due to shrinkage-driven flow. The results from the Al-4 wt pct Cu alloy are unreliable due to measurement issues. The relatively low eutectic percentage at the top of the Al-18 wt pct Cu 1 g sample is a result of floatation of grains. The Al-10 and 18 wt pct Cu 1 g samples both exhibit pockets of high eutectic fraction which can be attributed to gravity-driven transport.

D. EDX Macrosegregation Measurements

Two-dimensional maps of solute concentration, as measured by EDX, are shown in Figures 13, 14, 15. Recall that these are not the raw EDX measurements but sampled and square box averaged values that use a grid similar to the eutectic measurements. As before, the area within the black boundary is the same for both the EDX maps and the corresponding micrographs, and the box-values around the perimeter of the maps are all NaN. Large voids have been blacked out *via* NaN masking that was applied manually. Axial profiles of the diameter averaged solute concentration are provided in Figure 16.

The EDX measurements lead to mostly the same conclusions as the eutectic measurements. Although solute concentration and eutectic distribution are different quantities, they are directly related as the eutectic
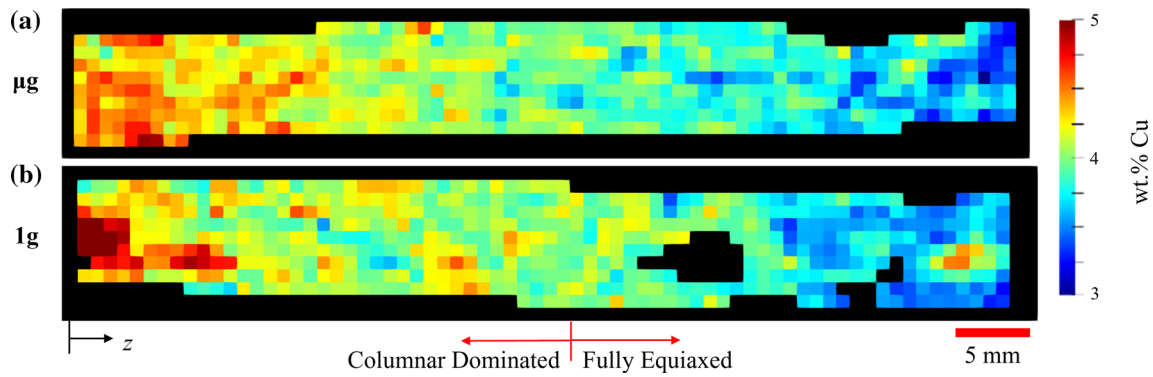
Fig. 13—Calibrated solute concentration maps for the Al-4 wt pct Cu (*a*) μg and (*b*) 1 g samples.
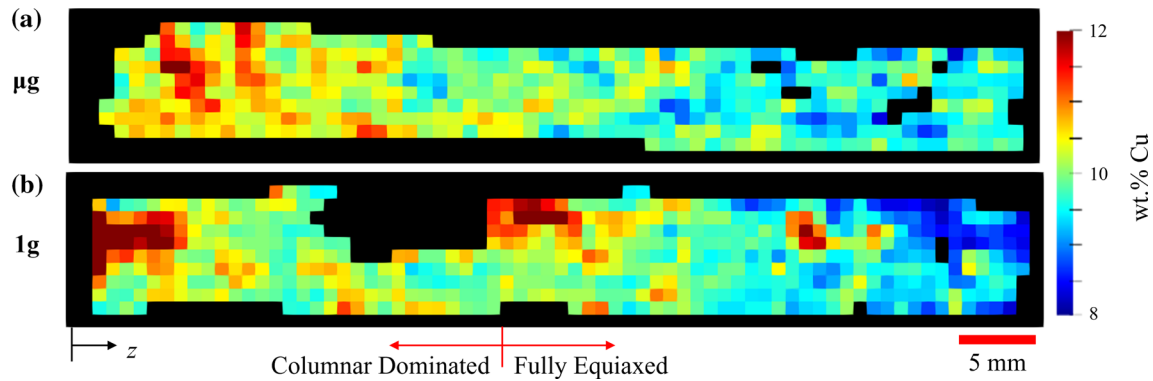

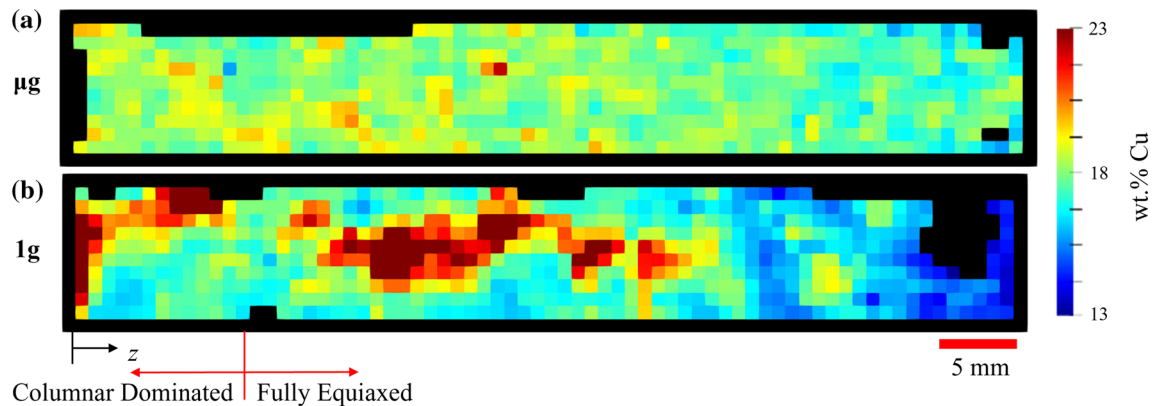Fig. 14—Calibrated solute concentration maps for the Al-10 wt pct Cu (*a*) μg and (*b*) 1 g samples.

Fig. 15—Calibrated solute concentration maps for Al-18 wt pct Cu (*a*) μg and (*b*) 1 g samples.

has a much higher solute concentration than the primary solid. As in the eutectic maps, EDX measurements for all μg cases in Figure 16 show evidence of inverse segregation, which is caused by shrinkage-driven flow and results in a decreasing solute concentration away from the chilled surface. The solute concentration maps for the 1 g samples contain additional features that are discussed below.

The Al-4 wt pct Cu μg and 1 g samples have highly similar macrosegregation profiles that both decrease steadily toward the sample end [Figure 16(a)]. Unlike

the eutectic fraction profiles in Figure 12(a), there is no sharp increase in the solute concentration profile near sample mid-height for the 1 g sample [Figure 16(a)]. This confirms that the eutectic measurements for the Al-4 wt pct Cu alloy are not reliable. The similarity of the 1 g and μg macrosegregation profiles indicates that melt convection and grain sedimentation have a negligible effect on the overall macrosegregation in the 1 g sample. Therefore, the solute concentration profile in the 1 g sample can be fully explained by shrinkage-driven flow. The only significant difference between
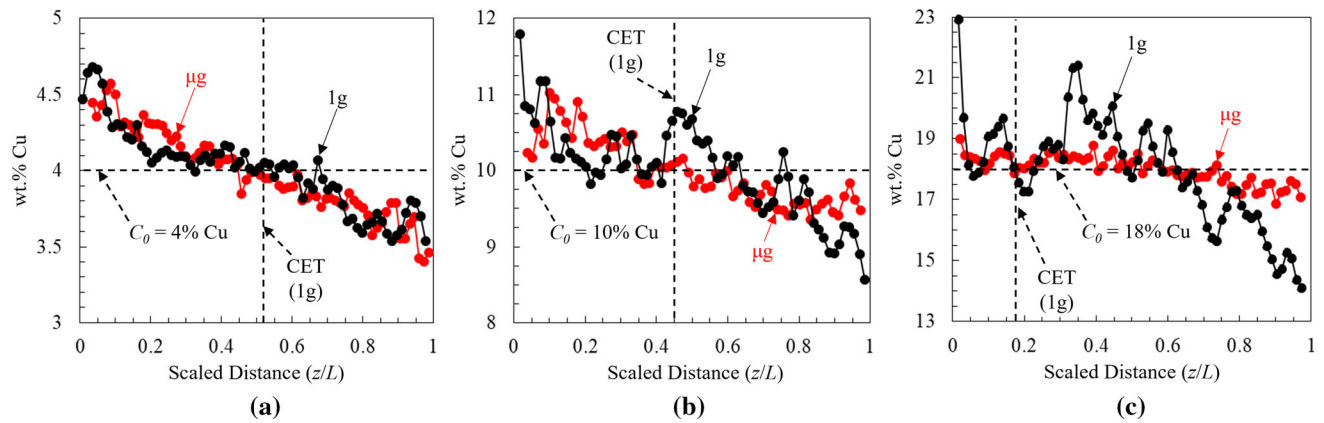
Fig. 16—Axial profiles of diameter averaged calibrated solute concentration for the (a) Al-4 wt pct Cu, (b) Al-10 wt pct Cu, and (c) Al-18 wt pct Cu samples.

the μg and 1 g samples is the presence of an isolated pocket of high solute concentration at the bottom of the 1 g sample in Figure 13(b), whereas the solute is more uniformly distributed over the cross section at that location in the μg sample in Figure 13(a). As before, this difference can be explained by melt convection during solidification.

The Al-10 wt pct Cu μg and 1 g samples both exhibit a similar pattern of inverse segregation [Figure 16(b)]. The overall similarity of the profiles indicates that gravity-driven transport of solute is not significant over the length of the 1 g sample. However, some non-uniformities in solute concentration over the cross section can be observed in the 1 g sample in Figure 16(b) that are not present for the μg sample in Figure 14(a). Pockets of positive solute segregation are visible in Figure 16(b) at the sample bottom, at the sample edge just above the large void, and in the sample cross section approximately 15 mm from the sample top. A pocket of negative segregation is visible at the top edge of the sample. These features are evidence of some melt convection within the 1 g sample.

The Al-18 wt pct Cu 1 g sample shows a far lower solute concentration at the sample top than the corresponding μg sample, which is apparent in both Figures 15 and 16(c). The μg sample solute profile shows a small and steady decrease from approximately 19 to 17 wt pct Cu over the sample length. On the other hand, the 1 g sample solute profile has a significant variation in solute concentration in the fully equiaxed region, ranging from approximately 22 to 14 wt pct Cu. The low solute concentration at the top of the 1 g sample can be attributed to grain floatation and the resulting accumulation of solute-poor primary solid at the top. The spikes in the 1 g sample solute concentration profile correlate with large areas of positive segregation that are non-uniform over the sample diameter. Pockets of positive segregation are visible at the sample bottom and along the sample edge in the columnar area of the 1 g sample. These pockets are evidence of melt convection. The large region of positive segregation along the axis in the fully equiaxed area is

likely due to a combination of grain floatation and melt convection.

The conclusions reached from the EDX measurements further support conclusions from the eutectic measurements. The similarity of μg and 1 g solute profiles indicates that most macrosegregation in all samples is caused by shrinkage-driven flow. Only the Al-18 wt pct Cu 1 g sample shows increased axial macrosegregation that can be attributed to grain floatation. All 1 g samples show pockets of high solute concentration which are indicative of melt convection during solidification.

E. Direct Comparison of Macrosegregation and Eutectic Measurements

In general, the macrosegregation patterns highly correlate with the corresponding eutectic fraction measurements for each alloy except for the Al-4 wt pct Cu 1 g sample. However, as discussed previously, the maps are only qualitatively comparable. In order to establish a direct quantitative comparison, the diameter averaged eutectic percentages were converted to solute concentrations using the rearranged Scheil equation in Eq. [2]. As before, the assumption of Scheil-type solidification is not valid for the 1 g samples with melt convection and solid transport. The transformed eutectic percentages and the EDX solute concentrations are normalized by their sample averages.

Figure 17 compares the normalized results of the two measurement methods. In general, the agreement between the two measurement methods is excellent. However, the Al-4 wt pct Cu normalized macrosegregation profiles in Figures 17(a) and (d) show moderate and poor agreement, respectively. This confirms that the eutectic measurements for the Al-4 wt pct Cu samples are unreliable for the reasons discussed earlier and, therefore, should be disregarded in favor of the EDX measurements. For the Al-10 and 18 wt pct Cu alloys, both methods produce the same significant spikes and overall variations in macrosegregation. Excellent agreement is particularly evident in the macrosegregation
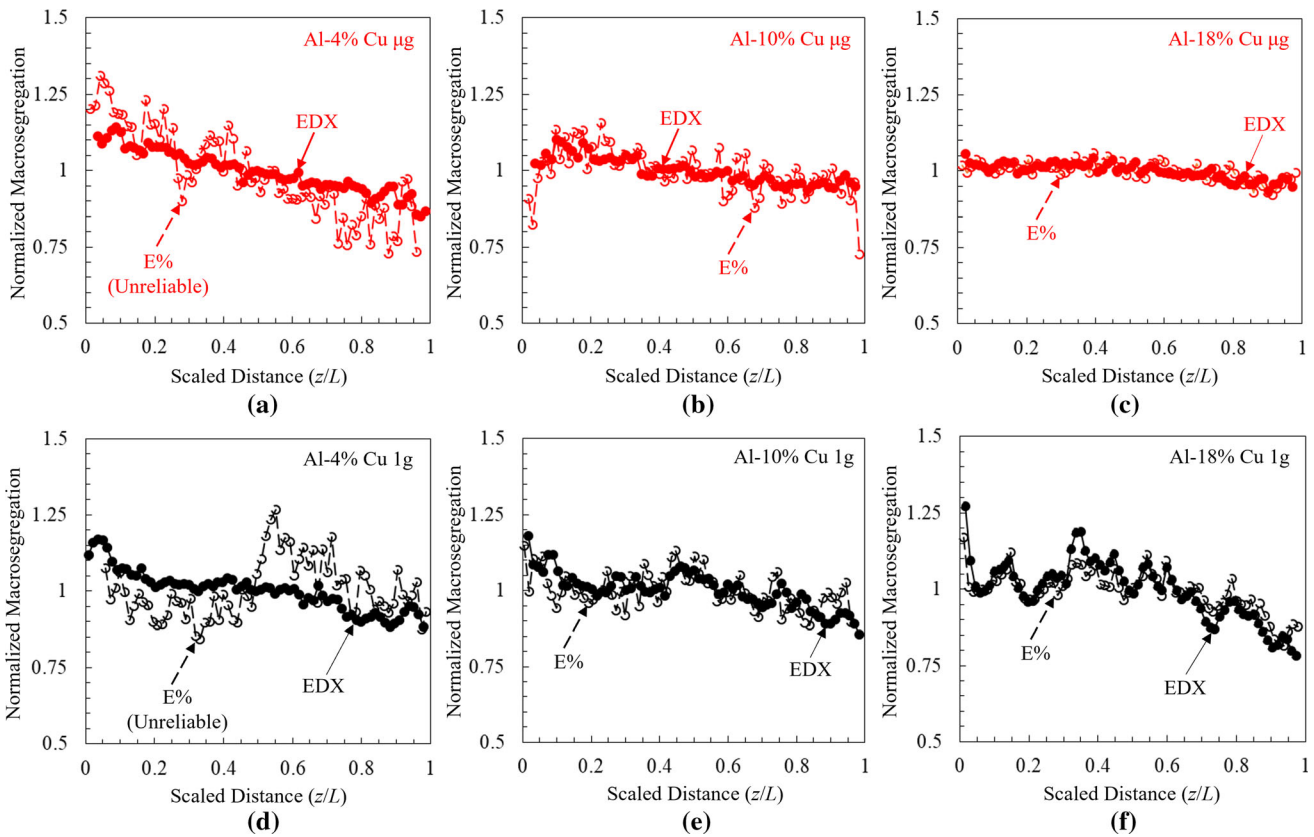
Fig. 17—Comparison of normalized macrosegregation profiles from eutectic fraction and EDX measurements for the (*a*) Al-4 wt pct Cu μg, (*b*) Al-10 wt pct Cu μg, (*c*) Al-18 wt pct Cu μg, (*d*) Al-4 wt pct Cu 1 g, (*e*) Al-10 wt pct Cu 1 g, and (*f*) Al-18 wt pct Cu 1 g samples. The eutectic measurements for the Al-4 wt pct Cu alloy samples are considered unreliable.

profiles for the 1 g samples in Figures 17(e) and (f) despite the limited validity of assuming Scheil-type solidification. The good agreement between the different measurement methods provides considerable confidence in each, except for the eutectic measurements in the Al-4 wt pct Cu alloy. Confidence in the macrosegregation measurements is critical to the use of the present experiments as a benchmark for modeling efforts.

IV. MODELING AND PROCESS CHARACTERIZATION

The temperature measurements recorded during the experiments are unsuitable for straightforward use as benchmark data due to the readings being taken on the exterior surface of the ampoule. There exists no temperature data taken directly on or in the alloy sample. Thermal boundary conditions on the sample surface are also necessary for future solidification modeling. In order to determine thermal boundary conditions and internal sample temperatures, a heat transfer model of the entire furnace including the sample is created. This furnace model is validated using the recorded temperatures from the experiments. Heat flux boundary conditions and internal temperatures are obtained from the furnace model. The boundary conditions are then applied to a sample-only heat diffusion model. The heat

flux boundary conditions are validated by comparing predicted internal temperatures between the sample and furnace models. The sample model is also used to track thermal process parameters along the axis for each sample for the microgravity cases.

A. Furnace Model

A model of the entire furnace, including the alloy sample, was constructed in the general-purpose casting simulation software MAGMAsoft.[38] This model is presented in full elsewhere,[37] and only a few key points are summarized here. The model cross section in Figure 1 is an illustration of the MAGMA model. Temperature-dependent thermophysical properties for the alloys are calculated using JMatPro, assuming Scheil-type solidification. These properties are included in the electronic supplementary spreadsheet in the online version of this article. Thermophysical properties for furnace and ampoule materials are based on literature values or MAGMA's own material database. The furnace and ampoule material properties are slightly adjusted to improve the accuracy of the model. The key to the model is replicating the variable heat input that limits the cooling rate of the furnace and sample ampoule. This is accomplished *via* the "heater" structure denoted in Figure 1. The heater consists of two parts: a hollow steel cylinder that represents the core of the

SUBSA furnace and three rings of constant temperature material that represent the resistive wire. The rings transfer heat to the steel cylinder only and are thermally isolated from other materials. The heat transfer from the rings to the cylinder is controlled by a time-dependent heat transfer coefficient (HTC) that mimics the variable heat input. The sample is modeled at the nominal length of 60 mm and diameter of 9 mm.

One simulation per alloy is conducted, as the μg and 1 g experiments were thermally identical. Only alloy properties and the time-dependent HTC are changed between simulations of the three different alloys. The samples are initialized as fully liquid at 900 °C and cooled to the temperature profile of the high temperature hold as heat transfer in the furnace approaches a steady state. Once the initial profile has been reached, cooling and solidification begin. Convection, solid transport, and solute transport are not considered in this model. An example of the excellent agreement between the temperatures predicted by the MAGMA model and those measured during the microgravity experiment is shown for the Al-4 wt pct Cu sample in Figure 18(a). Similarly good agreement is obtained for all alloys, as documented in Reference 37. It can be reasonably concluded that the furnace model is accurately representing the thermal conditions in the furnace, ampoule, and sample.

B. Thermal Boundary Conditions

Heat fluxes on the sample boundary are necessary for future modeling of the experiments. The sample cylinders are assumed to be axisymmetric, therefore top, bottom, and side boundary conditions are required. The heat fluxes through the top and bottom of the sample are assumed to be uniform in space while changing in time. The heat flux on the side of the sample, however, is spatially and temporally varying. To address this, the 6 cm long side boundary of the sample is divided into 12

discrete zones of 5 mm length each over which the heat flux is assumed to be uniform. The heat flux boundary conditions are calculated via a simple heat transfer analysis using temperatures extracted from the furnace model on either side of the sample-mold interface at the center of each zone. Including the top and bottom, 14 time-varying heat flux boundary conditions in total are determined from the MAGMA simulations for each sample. The initially calculated heat fluxes are then adjusted by 5 to 10 pct to produce good agreement between the internal temperatures predicted by the MAGMA furnace model and the thermal model of the sample, which is discussed in Sect. 4.3.

The heat fluxes determined for the Al-4 wt pct Cu sample are shown as an example in Figure 18(b) along with a key to their location on the sample surface. The complete set of time-dependent heat flux boundary conditions is available in Reference 37 and in the electronic supplementary spreadsheet online. It is clearly noticeable that most of the heat is removed through the bottom surface indicating that cooling in the sample is generally directional in nature. However, the lowest zone on the sample side does extract a non-negligible amount of heat from the sample. The remaining zones provide only a small amount of heating or cooling. At first, it may seem strange that there is heat input during the experiment. However, recall that the heater is not simply turned off but instead is actively modulated to control the furnace cooling rate.

C. Sample Model

A simple 2D axisymmetric model of the sample is created in the CFD simulation software OpenFOAM[39] in order to validate the heat flux boundary conditions. The domain used 22 cells across the 4.5 mm sample radius and 300 cells over the 60 mm length. The only equation of interest solved for the domain is the heat diffusion equation excluding the effects of convection
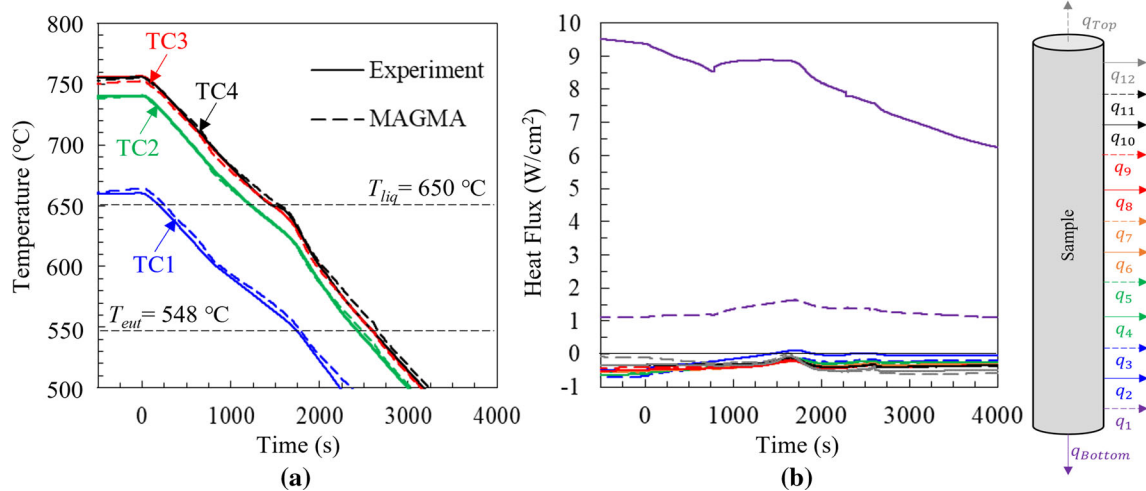

Fig. 18—An example of results from the furnace model for the Al-4 wt pct Cu sample: (a) predicted temperatures compared with the μg experimental results and (b) heat fluxes on the sample boundary; a key to the location of individual heat fluxes is provided to the right.

and transport of unattached solid. The temperature-dependent density, specific heat, and thermal conductivity are read directly from files containing tabulated thermophysical properties calculated by JMatPro. The latent heat is included within the specific heat term. The solid fraction is not directly used in the model; however, JMatPro assumes Scheil-type solidification when calculating the temperature-dependent thermophysical properties. Temperatures are probed along the axis at 1, 2, 4, and 5 cm from the sample bottom. The simulations were conducted with a timestep of 1 s.

The predicted temperatures are shown in Figure 19 and compared to those from the corresponding full furnace simulations. The sample model (OpenFOAM) shows excellent agreement with the furnace model (MAGMA) in all cases. Agreement is maintained through the liquidus and eutectic temperature arrests observed in Figure 18. This agreement validates the process used to extract heat fluxes from MAGMA as well as the resulting boundary conditions and their application to further modeling efforts. Again, the complete set of heat fluxes are provided in Reference 37 and in the electronic supplementary spreadsheet online. The temperatures in Figure 18 may be considered benchmark data for future models.

Thermal process parameters are also calculated from the sample model and are tracked along the sample axis. As there was no convection, solid transport, or solute transport modeled, the parameters are strictly applicable only to the experiments conducted in microgravity. While these parameters provide a reasonable overall characterization of the 1 g experiments, they should not be directly compared with results from models that account for any mass transport. Figure 20 shows the location history of the liquidus and eutectic isotherms along the sample axis. In all cases, the liquidus isotherm moves over the entire sample in approximately 700 s. There is a delay between when the liquidus isotherm reaches the end of the sample and when the sample bottom reaches the eutectic temperature that lasts 800, 600, and 200 s in the Al-4, 10, and 18 wt pct Cu cases respectively. During the delay, the mushy zone spans the entire sample width. This is likely a cause of the

significant inverse segregation that was observed in all samples. The eutectic isotherm traverses the length of the Al-4, 10 and 18 wt pct Cu samples in 300, 500, and 700 s, respectively. Figure 21 shows several thermal parameters tracked along the sample axis: the liquidus isotherm velocity, the temperature gradient in the axial direction at the liquidus isotherm, and the cooling rate at the liquidus isotherm. These parameters are tracked at the liquidus isotherm following other CET analyses such as Reference 30. The liquidus isotherm velocity [Figure 21(a)] is similar in all cases. The velocity is initially low but increases in the top 20 pct of the sample because the sample is nearly isothermal there. In general, the axial temperature gradient at the liquidus isotherm, shown in Figure 21(b), decreases toward the top of the sample. This is expected as the isotherm moves away from the lower cooling surface. All samples exhibit a similar reduction in axial temperature gradient along the sample length. Alloys with higher Cu concentration experience slightly higher temperature gradients. Although temperature gradients generally decrease along the sample, the axial temperature gradient initially increases from its value at 0 cm to a maximum value at about 0.7 cm. This is because the *axial* temperature gradient is being calculated rather than the radial temperature gradient or the total temperature gradient magnitude. Recall that the lowest part of the sample's side surface is also extracting heat while the rest of the side is inputting small amounts of heat. The maximum axial temperature gradient is located at the inflection point between heat extraction and input on the sample side. Cooling rates at the liquidus isotherm, shown in Figure 21(c), are generally low and decrease toward the sample top as expected. Alloys with higher Cu concentration experience slightly higher cooling rates.

V. CONCLUSIONS

Corresponding benchmark solidification experiments are performed in terrestrial and microgravity settings for end-cooled cylindrical samples of three Al-Cu alloys with negatively, neutrally, and positively buoyant
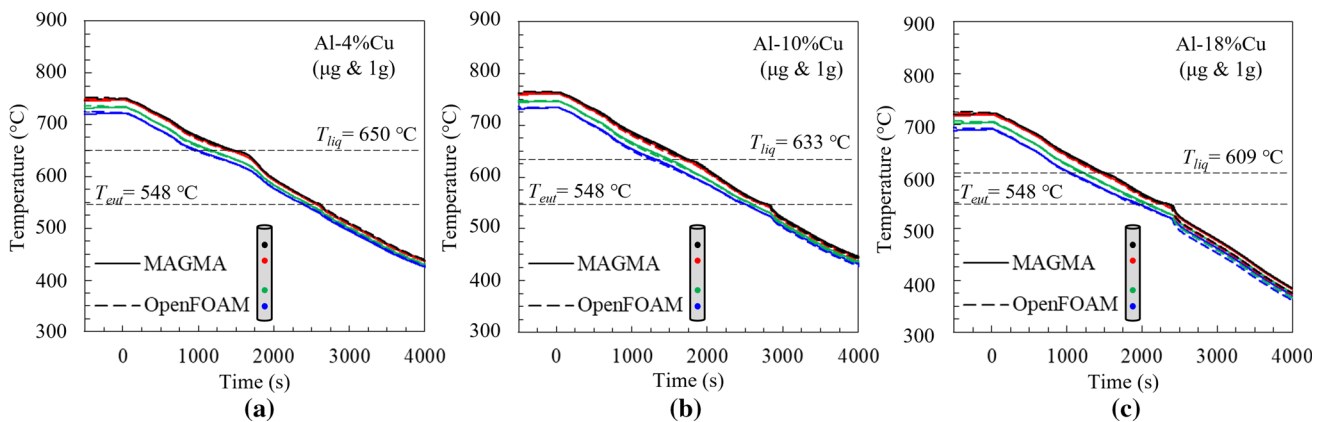
Fig. 19—Comparison of predicted temperatures between the MAGMA furnace model and the OpenFOAM sample model for the (*a*) Al-4 wt pct Cu, (*b*) Al-10 wt pct Cu, and (*c*) Al-18 wt pct Cu alloys. TC locations are on the sample axis 1, 2, 4, and 5 cm from the sample bottom.
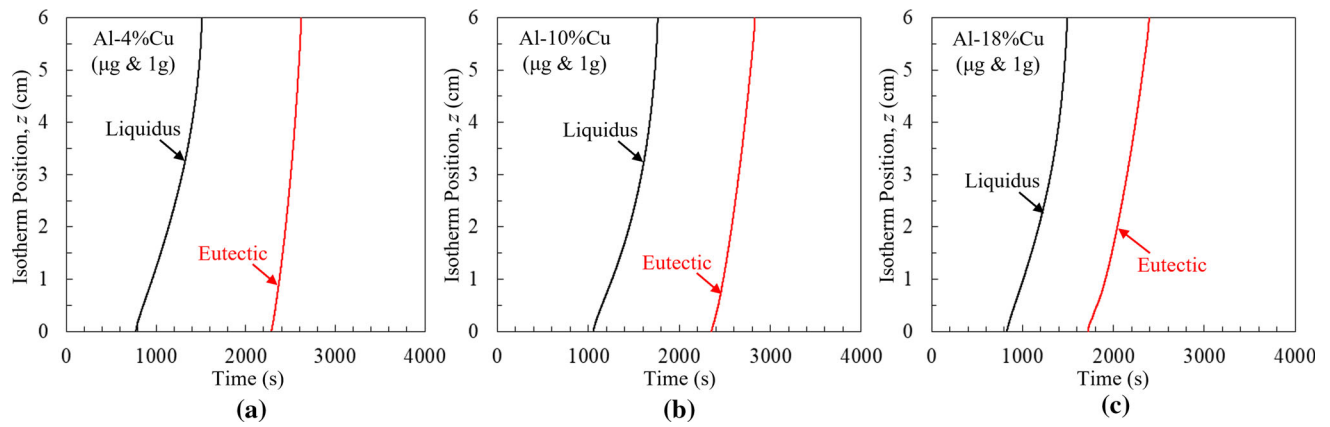
Fig. 20—Liquidus and eutectic isotherm location histories along the sample axis for the (*a*) Al-4 wt pct Cu, (*b*) Al-10 wt pct Cu, and (*c*) Al-18 wt pct Cu alloys.
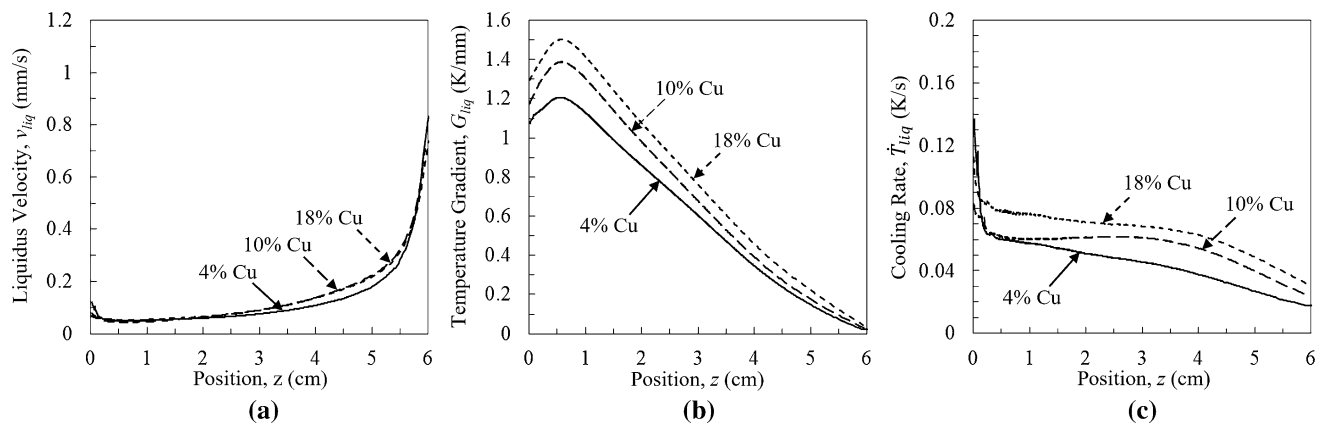

Fig. 21—Thermal process parameters evaluated at the liquidus isotherm along the sample axis: (*a*) liquidus velocities, (*b*) axial temperature gradients, and (*c*) cooling rates.

primary solid. All samples solidified in microgravity are entirely equiaxed while the samples solidified on Earth exhibit columnar growth near the chill surface. Columnar growth in the terrestrial samples is attributed to melt convection. In the terrestrially solidified alloy samples, the Al-4 and 18 wt pct Cu samples show evidence of grain sedimentation and floatation, respectively, while the Al-10 wt pct Cu sample does not exhibit any effects of transport of unattached grains.

All samples exhibit inverse segregation due to shrinkage-driven flow as demonstrated by the eutectic fraction and macrosegregation measurements. Shrinkage effects are therefore important to include in any future modeling efforts related to these samples. Samples solidified on Earth show pockets of high solute concentration and eutectic percentage that are evidence of melt convection. The terrestrially solidified Al-18 wt pct Cu sample exhibits negative solute segregation and low eutectic percentage at the top which is attributed to solute-poor primary solid grains floating to and accumulating there. Eutectic and macrosegregation measurements show excellent agreement with each other except for the

Al-4 wt pct Cu alloy. The high level of agreement in general indicates that the macrosegregation and eutectic fraction data can be confidently used as benchmarks, except in the case of the Al-4 wt pct Cu samples where only the macrosegregation measurements should be used.

Temperatures on the exterior surface of the ampoule are successfully predicted by a thermal model of the entire furnace. Heat flux boundary conditions on the sample surface are determined from the furnace model and validated using a second sample-only heat diffusion model. The boundary conditions are necessary for future modeling efforts. Selected predicted temperatures along the sample axis are presented as benchmark temperature data for the sample interior. In all samples, the liquidus isotherm passes through the full sample length before the eutectic isotherm begins to traverse the samples. Thermal process parameters calculated at the liquidus isotherm along the sample axis, including the isotherm velocity, axial temperature gradient, and cooling rate are similar in all samples.

The benchmark solidification data reported in this work are valuable for future modeling efforts. The data give the ability to validate combined models for grain structure and macrosegregation development in the presence of melt convection and transport of unattached solid. Models considering only diffusive processes and shrinkage can be validated using results from the microgravity experiments. The inclusion of the neutrally buoyant Al-10 wt pct Cu experiment allows for modeling solidification in the presence of gravity with minimal concern for buoyancy of the solid. The Al-4 and 18 wt pct Cu cases can then be used to validate models that account for transport of unattached grains.

CONFLICT OF INTEREST

On behalf of all authors, the corresponding author states that there is no conflict of interest.

SUPPLEMENTARY INFORMATION

The online version contains supplementary material available at https://doi.org/10.1007/s11661-022-06909-6.

REFERENCES

1. C. Beckermann and R. Viskanta: *PCH PhysicoChem. Hydrodyn.*, 1988, vol. 10, pp. 195–213.
2. M. Torabi Rad and C. Beckermann: *Materialia*, 2019, vol. 7, p. 100364.
3. J. Ni and C. Beckermann: *Metall. Trans. B*, 1991, vol. 22B, pp. 349–61.
4. C.Y. Wang and C. Beckermann: *Metall. Mater. Trans. A*, 1996, vol. 27A, pp. 2754–64.
5. C.Y. Wang and C. Beckermann: *Metall. Mater. Trans. A*, 1996, vol. 27A, pp. 2765–83.
6. C. Beckermann and C.Y. Wang: *Metall. Mater. Trans. A*, 1996, vol. 27A, pp. 2784–95.
7. M. Založnik and H. Combeau: *Comput. Mater. Sci.*, 2010, vol. 48, pp. 1–10.
8. M. Založnik, A. Kumar, and H. Combeau: *Comput. Mater. Sci.*, 2010, vol. 48, pp. 11–21.
9. L. Heyvaert, M. Bedel, M. Založnik, and H. Combeau: *Metall. Mater. Trans. A*, 2017, vol. 48A, pp. 4713–34.
10. M. Wu and A. Ludwig: *Acta Mater.*, 2009, vol. 57, pp. 5621–31.
11. M. Wu and A. Ludwig: *Acta Mater.*, 2009, vol. 57, pp. 5632–44.
12. M. Martorano, C. Beckermann, and C.-A. Gandin: *Metall. Mater. Trans. A*, 2003, vol. 34A, pp. 1657–74.
13. M. Wu, A. Fjeld, and A. Ludwig: *Comput. Mater. Sci.*, 2010, vol. 50, pp. 32–42.
14. M. Wu, A. Ludwig, and A. Fjeld: *Comput. Mater. Sci.*, 2010, vol. 50, pp. 43–58.
15. X.D. Wang and Y. Fautrelle: *Int. J. Heat Mass Transf.*, 2009, vol. 52, pp. 5624–33.
16. G. Quillet, A. Ciobanas, P. Lehmann, and Y. Fautrelle: *Int. J. Heat Mass Transf.*, 2007, vol. 50, pp. 654–66.
17. L. Hachani, B. Saadi, X.D. Wang, A. Nouri, K. Zaidat, A. Belgacem-Bouzida, L. Ayouni-Derouiche, G. Raimondi, and Y. Fautrelle: *Int. J. Heat Mass Transf.*, 2012, vol. 55, pp. 1986–96.
18. L. Hachani, K. Zaidat, B. Saadi, X.D. Wang, and Y. Fautrelle: *Int. J. Therm. Sci.*, 2015, vol. 91, pp. 34–48.
19. L. Hachani, K. Zaidat, and Y. Fautrelle: *Int J. Heat Mass Transf.*, 2015, vol. 85, pp. 438–454.
20. S. Ganesan and D.R. Poirier: *Metall. Trans. A*, 1987, vol. 18A, pp. 721–23.
21. H. Soltani, F. Ngomesse, G. Reinhart, M.C. Benoudia, M. Zahzouh, and H. Nguyen-Thi: *J. Alloys Compd.*, 2021, vol. 862, p. 158028.
22. H. Yasuda, Y. Yamamoto, N. Nakatsuka, M. Yoshiya, T. Nagira, A. Sugiyama, I. Ohnaka, K. Uesugi, and K. Umetani: *Int. J. Cast Met. Res.*, 2009, vol. 22, pp. 15–21.
23. R.S. Rerko, H.C. de Groh III, and C. Beckermann: *Mater. Sci. Eng. A*, 2003, vol. 347, pp. 186–97.
24. G. Zimmermann, C. Pickmann, M. Hamacher, E. Schaberger-Zimmermann, H. Neumann-Heyme, K. Eckert, and S. Eckert: *Acta Mater.*, 2017, vol. 126, pp. 236–50.
25. M.H. Burden, D.J. Hebditch, and J.D. Hunt: *J. Cryst. Growth*, 1973, vol. 20, pp. 121–24.
26. G. Reinhart, C.-A. Gandin, N. Mangelinck-Noël, H. Nguyen-Thi, J.-E. Spinelli, J. Baruchel, and B. Billia: *Acta. Mater.*, 2013, vol. 61, pp. 4765–77.
27. H. Nguyen-Thi, G. Reinhart, G. Salloum Abou Jaoude, R.H. Mathiesen, G. Zimmermann, Y. Houltz, D. Voss, A. Verga, D.J. Browne, and A.G. Murphy: *J. Cryst. Growth*, 2013, vol. 374, pp. 23–30.
28. A.G. Murphy, R.H. Mathiesen, Y. Houltz, J. Li, C. Lockowandt, K. Henriksson, N. Melville, and D.J. Browne: *J. Cryst. Growth*, 2016, vol. 454, pp. 96–104.
29. F. Ngomesse, G. Reinhart, H. Soltani, G. Zimmermann, D.J. Browne, W. Sillekens, and H. Nguyen-Thi: *Acta Mater.*, 2021, vol. 221, p. 117401.
30. D.R. Liu, N. Mangelinck-Noël, C.-A. Gandin, G. Zimmermann, L. Sturz, H. Nguyen-Thi, and B. Billia: *Acta Mater.*, 2014, vol. 64, pp. 253–65.
31. Y.Z. Li, N. Mangelinck-Noël, G. Zimmermann, L. Sturz, and H. Nguyen-Thi: *J. Cryst. Growth*, 2019, vol. 513, pp. 20–29.
32. R.A. Spivey, S. Gilley, A. Ostrogorsky, R. Grugel, G. Smith, and P. Luz: *AIAA Pap.*, 2003, vol. 1362, pp. 1–10.
33. M. Bedel, K.O. Tveito, M. Zaloznik, H. Combeau, and M. M'Hamdi: *Comput. Mater. Sci.*, 2015, vol. 102, pp. 95–109.
34. N. Saunders, Z. Guo, X. Li, A.P. Miodownik, and J.-P. Schillé: *JOM*, 2003, vol. 55, pp. 61–65.
35. J.A. Dantzig and M. Rappaz: *Solidification*, 1st ed. EPFL Press, Lausanne, 2009.
36. C.A. Schneider, W.S. Rasband, and K.W. Eliceiri: *Nat. Methods*, 2012, vol. 9, pp. 671–75.
37. T.J. Williams: PhD Thesis, The University of Iowa (2022).
38. MAGMAsoft, MAGMA Gmbh, Kackerstrasse 16–18, 52072 Aachen, Germany.
39. OpenFOAM v9 user guide. (The OpenFOAM Foundation, 2022), https://cfd.direct/openfoam/user-guide. Accessed 14 June 2022.